Marine Pollution Bulletin 144 (2019) 265–274

Contents lists available at ScienceDirect

Marine Pollution Bulletin

journal homepage: www.elsevier.com/locate/marpolbul

On relaxation of the influences of treated sewage effluent on an adjacent seaweed farm in a tidal strait

Xu Zhang[a,*], Yusuke Uchiyama[a,b], Akihiko Nakayama[c]

[a] Department of Civil Engineering, Kobe University, Kobe, Japan
[b] Coastal and Estuarine Environmental Department, Port and Airport Research Institute, Yokosuka, Japan
[c] Department of Environmental Engineering, Universiti Tunku Abdul Rahman, Kampar, Perak, Malaysia

ARTICLE INFO

Keywords:
Treated wastewater effluent
Alternative operation
Coastal dispersal
Transient effluent flux
Tidal strait
ROMS

ABSTRACT

An Eulerian passive tracer model coupled with a quadruple-nested 3D circulation model was used to assess the coastal dispersal of treated wastewater effluent from a sewage treatment plant and the associated impacts on an adjacent seaweed farm using three different operational scenarios. When the discharged volume and source effluent fluxes were decreased by ~16.7%, the accumulated effluent in the farm was reduced by ~25.4%. A tracer flux budget analysis revealed the apparent predominance of the transient component that accounts for the nonlinear interactions primarily from tidal currents and eddies. The transient flux promoted the effluent influx to impede effluent accumulation in the farm, whereas the mean flux contributed to the outgoing flux. A source flux reduction caused a remarkable decrease in the transient flux and thus an even greater effluent accumulation reduction. In turn, a modified source density scenario without total effluent volume change did not work as expected.

1. Introduction

Osaka Bay is located in the northeastern area of the Seto Inland Sea (SIS), Japan, that is the largest estuary in the nation and forms a typical 'basin-strait' system. Osaka Bay consists of a shallow inner bay and a deep channel that is connected with the neighboring two sub-basins, Harima Sea and Kii Channel, by the narrow Akashi and Kitan straits (Fig. 1). The subtidal residual circulations in the SIS and Osaka Bay primarily occur in the clockwise direction under substantial remote influences from the Kuroshio drifting eastward off the Kii Channel and its occasional intrusions into the SIS (Takeoka et al., 1993; Tada et al., 2018) and meandering of the Kuroshio path (e.g., Kawabe, 1987, 1995). Concurrently, strong tidal currents bring water back and forth to Osaka Bay through the straits at a maximum speed of 3 m s^{-1} through the Akashi Strait (Fujiwara et al., 1994). In this type of basin-strait system, the water is well mixed near the straits, while it is stratified in the inner basins (e.g., Guo et al., 2004; Chang et al., 2009). 'Red tides' are an indicator of harmful algal blooms followed by hypoxia. Historically, these have occurred quite frequently in Osaka Bay mostly during the boreal summer and fall, resulting in serious water quality deteriorations that damage the aquaculture and marine ecosystem (e.g., Imai et al., 2006; Terawaki et al., 2003). Accordingly, several ecological shifts have been reported to occur in this densely populated region (Irizuki et al., 2018). A series of environmental preservation policies and laws have been enacted to limit the total amount of nutrients in treated wastewater effluents. These measures have adequately succeeded in improving the water quality in recent years in the SIS (Tomita et al., 2016). However, Osaka Bay still suffers from severe water pollution due to a vast amount of sewage from the densely populated hinterland.

The Tarumi Sewage Treatment Plant (TSTP) is one of the largest wastewater treatment plants in Osaka Bay, collocated with the second largest productive seaweed farm in the nation. The local farmers association continually claims that the treated wastewater effluent derived from the TSTP may result in severe reductions in the quality and production of the seaweed farm located next to the TSTP. To alleviate possible undesirable TSTP influences on the local aquaculture, the City of Kobe Sanitation Bureau (hereafter KSB), the local government, has constructed an alternative western diversion outfall (Fig. 1c; indicated by "W") 500 m away from the original TSTP central outfall (Fig. 1c, "C"). The TSTP has thereby conducted seasonal diversions from October to December when the seaweed spores are the most sensitive to the ambient marine environment.

In our previous study (Uchiyama et al., 2018a), we conducted a quantitative assessment of the impacts of the western diversion discharge relative to the hypothetical central outfall discharge in the fall

* Corresponding author.
E-mail address: 167t142t@stu.kobe-u.ac.jp (X. Zhang).

https://doi.org/10.1016/j.marpolbul.2019.04.050
Received 19 February 2019; Received in revised form 11 April 2019; Accepted 19 April 2019
Available online 16 May 2019

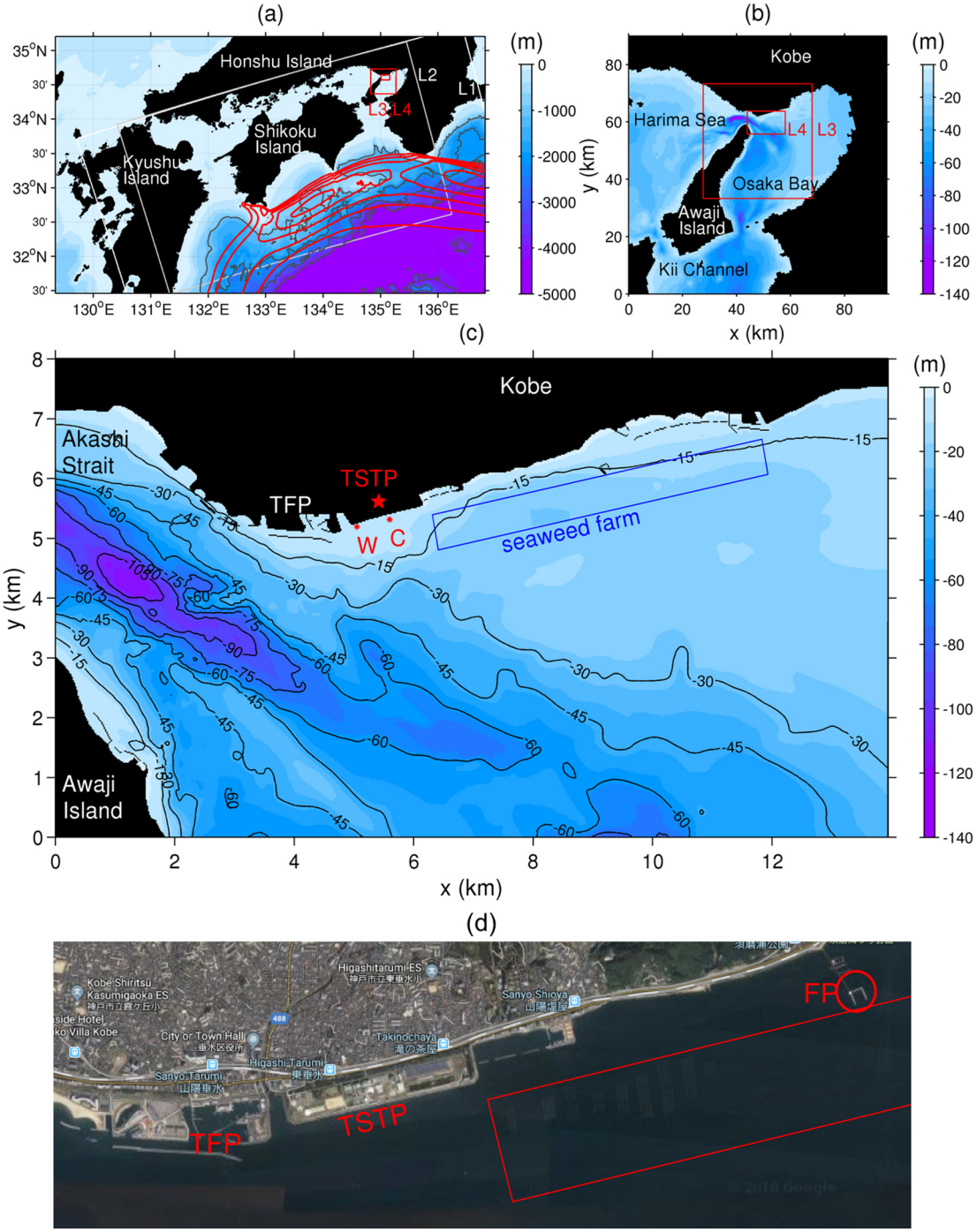

Fig. 1. Quadruple-nested JCOPE2-ROMS model domains and bathymetry (color: m). (a) The ROMS-L1, L2 (white boxes), L3, and L4 domains (red boxes) embedded in the JCOPE2 domain (outside of the perimeter of the L1). The gray contours are the isobaths with 1000 m intervals, while the red contours indicate the approximate Kuroshio region with the surface velocity magnitudes > 0.5 m s^{-1} at 0.2 m s^{-1} intervals. (b) The enlarged region around Osaka Bay including the ROMS-L3 and L4 domains (red boxes). (c) The entire L4 domain with isobaths at 15 m intervals. The blue box is the approximate extent of the seaweed farm area of interest; TFP is the Tarumi Fishery Port; the red star shows the location of the Tarumi Sewage Treatment Plant (TSTP); the red dots are the two outfalls (W: western diversion outfall, C: central original outfall). (d) Aerial photo around the TSTP from Google map. The seaweed farm (red box), TSTP, and TFP are indicated on the figure. The local fishing pier (FP) construction is shown by the red circle. (For interpretation of the references to color in this figure legend, the reader is referred to the web version of this article.)

condition based on a 3D numerical ocean circulation model. Uchiyama et al. (2018a) concluded that the diversion operation successfully decreased the accumulation of the TSTP effluents in the adjacent farm by on average ~28%, while the instantaneous effluent concentration was reduced to ~50%. The time-averaged horizontal effluent concentration derived either from the central or western outfall was distributed asymmetrically with a westward-stretched, coastally trapped shape, leading to the reduction of effective accumulation in the farm. The high-resolution numerical model used in Uchiyama et al. (2018a) provided solid explanations for the mechanism behind such non-Gaussian distributions and has been validated comprehensively against in-situ measurements and the observations of Bricker et al. (2006) and

Bricker and Nakayama (2007), as briefly described below. Overall, the effluent is transported due to tidal and subtidal residual currents that are largely dominant in the coastal area around the TSTP and the adjacent seaweed farm. The tidal currents occur more intensively near the outfall (the western area of the farm) causing both cross-shore and along-shore effluent transports, although the subtidal currents are more influential leaving westward from the Akashi Strait where the energetic tidal currents occur. The cross-shore currents are pronouncedly developed more by the tidal oscillations with noticeable influences from low-frequency wind stress variations than from the alongshore currents. The key influencer on the anisotropic effluent distribution is the subtidal counterclockwise circulation that brings effluents westward and then southward 2–3 km west of the outfall to the offshore.

Even though the diversion operation was numerically assessed such that it would function properly in terms of reducing effluent accumulations in the seaweed farm, the farmers are still demanding that the KSB should further diminish the TSTP influence with minimal additional costs. Hence, the KSB has proposed two possible alternative operational scenarios using the diversion outfall. The first option is simply to lower the freshwater effluent discharge volume without the nutrient concentration adjustments (discharged total nutrient load is also lowered proportionally with the effluent volume). The second is to increase the effluent density by mixing the treated fresh wastewater with the ambient saline seawater while retaining the nutrient total mass. Both operational scenarios are not only practically plausible, but also scientifically intriguing to pursue. According to Uchiyama et al. (2018a), it is presumed that the anisotropic subtidal circulation may invoke nonlinear proportionality between the effluent volume and the resultant accumulation in the farm during the first scenario. By contrast, the second scenario is expected to weaken the near-field vertical buoyant plume from the bottom-mounted diffusers of the diversion outfall, and this would presumably alter the vertical distribution of the nutrients at the source location and subsequent far-field lateral dispersal.

Therefore, this study aimed to provide scientific insights and qualitative guidelines on the alternative discharge operations for reducing the TSTP influence on the farm. To this end, we conducted a detailed numerical assessment based on the high-resolution 3D model developed in Uchiyama et al. (2018a) using the two proposed scenarios. Our 3D model accounts for the driving mechanisms responsible for the present assessment as realistically as possible. For instance, the model considers large-scale effects including the remote influences from the Kuroshio that determines the eastward residual current in the SIS (so-called the SIS throughflow; Tada et al., 2018), spatiotemporally varying atmospheric forcing (sea surface wind stress, radiation, and heat fluxes), high-frequency intrinsic variabilities such as barotropic and baroclinic tides, and freshwater inputs from both precipitation and rivers. The remainder of the paper is organized as follows. The model design and configurations for constructing the proposed operational scenarios are briefly described in Section 2. Section 3 illustrates the near-surface horizontal hydrodynamic and effluent concentration fields formed around the TSTP and the seaweed farm, and a quantitative assessment of the TSTP influences on the seaweed farm in the two scenarios is conducted in this section based on an effluent flux budget analysis, with comparisons to the standard discharge operation with the western diversion outfall. The conclusions are provided in Section 4.

2. Methods

2.1. The ocean circulation model

We employed a 3D Eulerian passive tracer model with a near-field dilution sub-model (Uchiyama et al., 2014) to compute a 3D dispersal of the buoyant plume representing the effluent derived from the TSTP western diversion outfall (see Sec. 2.2). The tracer model was driven by the 3D velocity and eddy diffusivity estimated using the innermost child model of the quadruple-nested downscaling Regional Oceanic Modeling System (ROMS; Shchepetkin and McWilliams, 2005, 2008). The lateral boundary conditions for the outermost ROMS-L1 model were acquired from the assimilative Japan Coastal Ocean Predictability Experiments (JCOPE2) oceanic reanalysis (Miyazawa et al., 2009). The one-way offline nesting technique (e.g., Mason et al., 2010; Buijsman et al., 2012; Romero et al., 2013; Uchiyama et al., 2010, 2017a, 2017b, 2017c, 2018b; Kamidaira et al., 2017, 2018) was utilized to successively convey the parent model results into the child models with grid-size refinements (i.e., JCOPE2 at a lateral grid resolution of ~10 km → L1 at 2 km → L2 at 600 m → L3 at 100 m → L4 at 20 m). Thus, the innermost ROMS-L4 model domain was discretized horizontally at 20 m lateral grid spacing, and vertically into stretched 32 *s*-layers. The ROMS configurations were the same as those in Uchiyama et al. (2018a). For instance, the L4 model was forced using the surface wind stress data from the Japan Meteorological Agency (JMA) Grid-Point Values–MesoScale Model (GPV-MSM; Isoguchi et al., 2010) and the surface heat/freshwater fluxes from the Comprehensive Ocean-Atmosphere Data Set (COADS; Woodruff et al., 1987). Along the L2 model open boundaries, the barotropic tides were synthesized from ten constituents acquired from the TPXO7.0 global reanalysis (Egbert et al., 1994; Egbert and Erofeeva, 2002) that spontaneously generated the intrinsic barotropic and baroclinic tides that were transmitted through the open boundaries into the L3 and L4 models. Because the seaweed spores are sensitive to both salinity and nitrate, the impacts of freshwater from the local rivers are worth considering. Therefore, freshwater discharge from all the major rivers located in the model domains was also taken into account as monthly-averaged freshwater volume fluxes. The ROMS-L4 model was run for approximately 50 days to include October 2015 when the seaweed spores were the most sensitive to the effluent. Table 1 summarizes the detailed numerical configurations for the ROMS-L1-L4 models. Further details of the model design can be found in Uchiyama et al. (2018a).

Table 1
Model configurations.

Models	L1	L2
Computational period	3/1/2006–11/31/2015	9/1/2006–11/9/2015
Grid cells	320 × 320 (×32 layers)	800 × 480 (×32 layers)
Horizontal grid resolution	2 km	600 m
Baroclinic time step	120 s	30 s
Surface wind stress	JMA-MSM (hourly)	JMA-MSM (hourly)
Surface flux	COAMPS bulk formula	COAMPS bulk formula
Boundary/Initial condition	JCOPE2 (daily)	ROMS-L1 (daily)
T-S nudging	JCOPE2 (10-day averaged)	None
Topography	SRTM30 + JEGG500	SRTM30 + JEGG500

COAMPS: Coupled Ocean/Atmosphere Mesoscale Prediction System (Hodur, 1997)
STRM30: SRTM30_PLUS (Rodriguez et al., 2005; Rodriguez et al., 2006; Becker et al., 2009)
J-EGG500 (http://www.jodc.go.jp/data_set/jodc/jegg_intro.html)

Models	L3	L4
Computational period	9/1/2015–11/9/2015	9/21/2015–11/9/2015
Grid cells	400 × 400 (×32 layers)	696 × 400 (×32 layers)
Horizontal grid resolution	100 m	20 m
Baroclinic time step	8.0 s	1.0 s
Surface wind stress	JMA-MSM (hourly)	JMA-MSM (hourly)
Surface flux	COADS (monthly climatology)	COADS (monthly climatology)
Boundary/Initial condition	ROMS-L2 (hourly)	ROMS-L3 (hourly)
T-S nudging	None	None
Topography	CDPC	CDPC

CDPC: Central Disaster Prevention Council, Japan (50 m resolution).

Table 2
Different discharge operations scenarios.

	Sewage volume (m^3/d)	Mixing seawater (m^3/d)	Salinity (psu)	Density (kg/m^3)
Case 1: baseline	1.8×10^5	None	0	997.55
Case 2	1.5×10^5	None	0	997.55
Case 3	1.8×10^5	8×10^4	10.46	1005.43

Note: the mean temperature was as that of ambient seawater at 23 °C. The surface salinity and density of the seawater were 34.4 psu and 1023.48 kg m^{-3}, respectively.

2.2. The sewage effluent model

The 3D sewage effluent oceanic dispersal in the L4 domain was modeled as a conservation equation of the non-dimensional Eulerian passive tracer concentration c with the near-field dilution sub-model (Uchiyama et al., 2014, 2018a):

$$\frac{\partial c}{\partial t} + \nabla \cdot \mathbf{u}c = \mathscr{D} + \mathscr{P} \tag{1}$$

where the near-field dilution is represented as the non-dimensional source term, $\mathscr{P}$:

$$\mathscr{P}(x, y, z; t) = P_s(t) A(x, y) H(z) \tag{2}$$

where $\mathbf{u}$ is the 3D velocity of the ambient flow, $\mathscr{D}$ is the diffusion term, ∇ is the 3D gradient operator, P_s is the tracer flux from the outfall, and A and H are the non-dimensional spatial plume shape functions above the bottom-mounted diffusers. The shape functions A and H were utilized to represent the source region spatial distribution as shown in the following integral relations:

$$\iint A dxdy = A_s, \int H dz = H_s \tag{3}$$

where A_s is the horizontal area, H_s is the vertical size, and $V_s = A_s H_s$ is the sewage plume volume. Hence, $P_s(t) = Q_p(t)/V_s$, where Q_p (t) [$m^3 s^{-1}$] is the volume flux. The dimensional pollutant concentrations were retrieved using cC_p, where C_p is the input pollutant concentration at the outfall. Note that a similar source term is added to the 3D mass, momentum, salinity, and temperature conservation equations to account for the near-field dilution effects.

The shape functions A and H are described also according to Uchiyama et al. (2014). A Gaussian distribution model,

$$H(z) = \exp\left[-\frac{(z - z_s)^2}{d_s^2}\right] \tag{4}$$

was used for the vertical function H, where z_s is the plume center height, and d_s is the vertical scale of the plume. We defined $z_s = 0$ m and $d_s = 7$ m as the buoyant effluent was released from the bottom-mounted diffusers of the TSTP diversion outfall at a mean depth of 7 m. This depth is shallower than the local mixed layer depth, and thus the released buoyant effluent immediately reaches the surface, regardless of choice of the shape functions and model parameters. The outfall was represented by two grid points with a footprint of 20 m × 40 m, where $A = 0.5$, centered 40 m offshore from the TSTP sea wall, approximately corresponding to the actual diversion outfall design.

2.3. The standard and two alternative operation scenarios

The sewage effluent was applied to the coastal area near the TSTP as a bottom-released freshwater plume at the volume rate of Q_p with a prescribed concentration of $c = c_s$, yielding a source tracer flux at the outfall of $F_p = c_s Q_p$. The discharged hypothetical passive tracer was set to unity ($c_s = 1$) with the temperature of the ambient seawater, unless otherwise stated. For the standard diversion operation (Case 1: the baseline case), a constant volume rate $Q_p = 1.8 \times 10^5\ m^3\ d^{-1}$ and zero salinity were imposed. The mean seawater surface temperature and salinity near the outfall were 23.0 °C and 34.4 psu. Hence, at 23.0 °C, the resultant mean density was 1023.48 kg m^{-3}, while the freshwater density was 997.55 kg m^{-3}.

The two alternative operations proposed by the KSB (Section 1) were then configured on the basis of the Case 1 experimental set-up. The first alternative was simply a reduced Q_p discharge volume from $1.8 \times 10^5\ m^3\ d^{-1}$ to $1.5 \times 10^5\ m^3\ d^{-1}$ with the other conditions retained (Case 2: the reduced Q_p case). Hence, the F_p source tracer flux was also lowered at the same reduction rate as the Q_p with $c_s = 1$. In the second scenario, the effluent density was increased by mixing with $0.8 \times 10^5\ m^3\ d^{-1}$ of the ambient seawater to suppress the buoyant plume from surfacing during the initial dilution (Case 3: the increased density case). As a consequence, the total Q_p discharge rate, the density of the mixed effluent ρ', and its salinity S' were modified in Case 3 to $Q_p = 2.6 \times 10^5\ m^3\ d^{-1}$, $\rho' = 1005.43$ kg m^{-3}, and $S' = 10.46$ psu, respectively. We further modified the source tracer flux $c_s = (1.8 \times 10^5) / (2.6 \times 10^5) \sim 0.69$ such that the total tracer load from the TSTP for Case 3 was equal to Case 1, even with the seawater addition and density alteration. The vertical shape function H was not altered in all three cases as defined in Section 2.2. The model configurations for the three cases are summarized in Table 2.

3. Results and discussion

3.1. Residual currents

In basin-strait systems, tides are known to be the most influential factors to affect currents particularly near straits with intensive fluctuations at relatively small spatiotemporal scales (e.g., Imasato, 1983; Imasato et al., 1994; Li et al., 2015). The present study area is in a location where strong tidal currents are generated in the narrow Akashi Strait that could affect the transport and dispersal of sewage effluents from the TSTP. Strong tidal currents are repeatedly generated at the narrow Akashi Strait. Fig. 2a shows the surface residual currents in Case 1 estimated for the entire experimental period from September 21st to October 31st, 2015. Overall, the strong southeastward residual currents occur and intrude into Osaka Bay through the Akashi Strait. These residual currents involve three major circulations. The largest is a clockwise circulation formed as a part of the well-known 'Okinose Circulation' (e.g., Nakatsuji et al., 1994; Mishima et al., 1999) that appears as a semi-circle with the origin at approximately $(x, y) = (4$ km, 0 km). Consistent with the findings in Imasato (1983), the intermediate counterclockwise circulation (hereafter termed the 'Tarumi Recirculation') develops with the prominent westward alongshore current near the TSTP. The smallest local recirculation is instigated off the northern coast of the Akashi Strait. The two counter-rotating larger circulations converge at around $(x, y) = (4$ km, 4 km) and develop into the intensive southeastward current. In turn, the strongest northwestward current occurs along the northern coast of Awaji Island and then veers clockwise at two locations in the Akashi Strait to form two clockwise circulations including the Okinose Circulation. As was reported in Uchiyama et al. (2018a), the Tarumi Recirculation is substantially important for promoting the mean westward transport of effluent from the TSTP that is ultimately responsible for reducing effluent accumulations in the seaweed farm using the diversion operation.

It is worth mentioning that the velocity vectors in Fig. 2a are

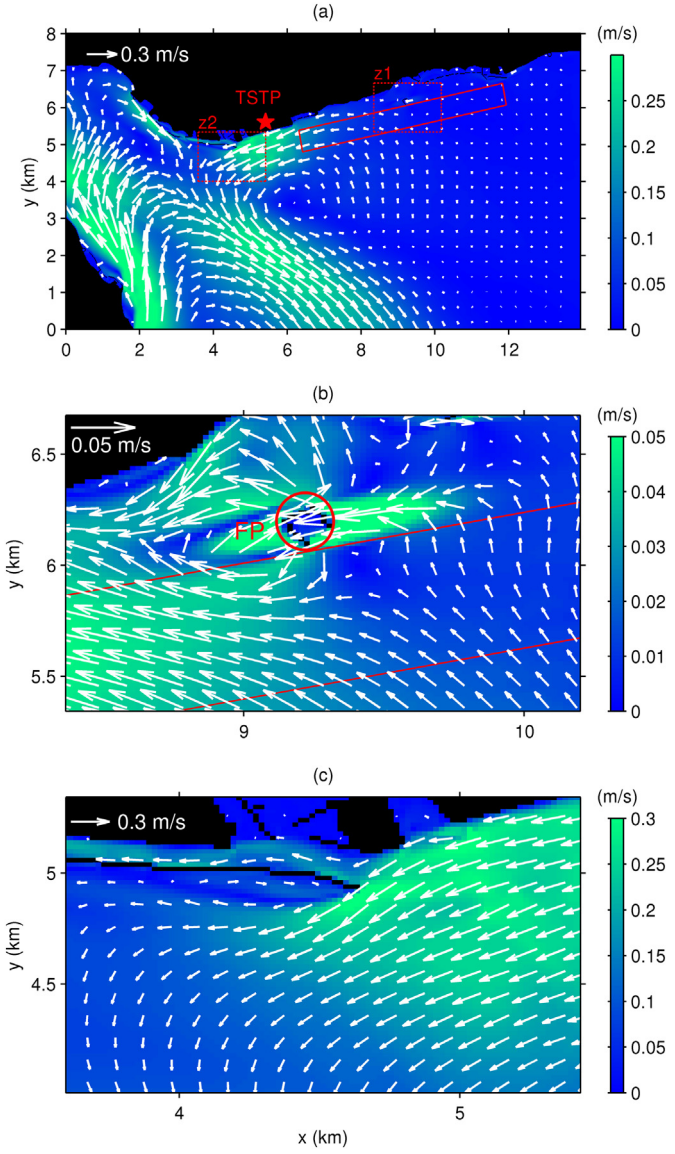

Fig. 2. (a) Time-averaged surface velocity vectors (white arrows) on their own magnitude (color). (b) Same as (a) but for the enlarged region shown by the red dotted box (z1) in Fig. 2a. The location of the fishing pier (FP) construction is shown by the red circle. (c) Same as (a) but for the enlarged region shown by the red dotted box (z2) in Fig. 2a. The red solid box shows the seaweed farm area. (For interpretation of the references to color in this figure legend, the reader is referred to the web version of this article.)

subsampled every 20 grids, resulting in lack of the detailed flow structures that should be observable in the ROMS-L4 model outcome with a lateral grid resolution of 20 m. Two selected enlarged regions shown in Fig. 2b-c demonstrate the influences of man-made marine constructions in the red dotted boxes labeled with z1 and z2 in Fig. 2a, where the velocity vectors were then subsampled every 5 grids. We now see the complex residual current field around the foundation of a fishing pier (indicated as "FP" in Fig. 1d) in Fig. 2b. The pier has significant effects on the local residual currents, where zonal divergence occurs with obvious opposing eastward flows in the downstream region. The southward transport is formed locally near the pier crossing the northern perimeter of the seaweed farm depicted by the red line. On the western area of the TSTP, the Tarumi Fishery Port ("TFP" in Fig. 1d) breakwater provokes a bifurcation of the westward coastal residual current with noticeable velocity weakening, southward veering, and a tiny local clockwise recirculation along the southern side (Fig. 2c).

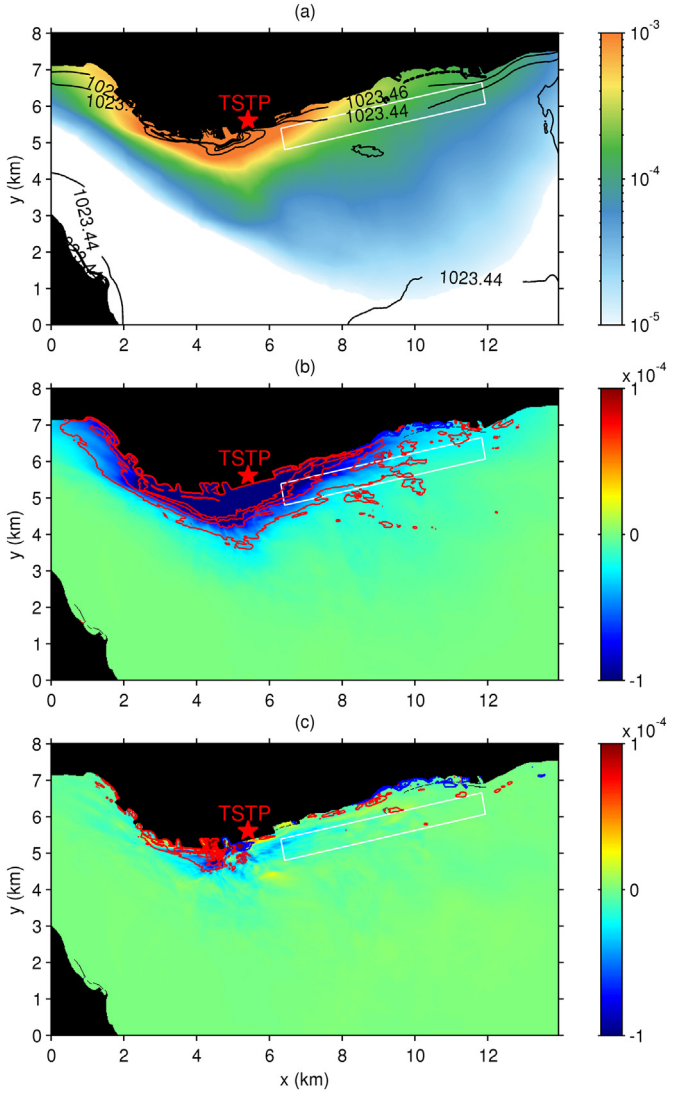

Fig. 3. (a) Time-averaged passive tracer concentration, c (color, non-dimensional) at the surface for the baseline case (Case 1). The black contours denote the sea surface density at 0.02 kg m^{-3} intervals. (b) The differences in c (color, non-dimensional) and density (contours) between Case 2 and Case 1 (Case 2 − Case 1). The red and blue contours are positive and negative values (intervals: 0.001 kg m^{-3}). (c) Same as (b), but for Case 3 − Case 1. (For interpretation of the references to color in this figure legend, the reader is referred to the web version of this article.)

3.2. Time-averaged density and effluent concentrations

As the seaweed is cultivated near the surface for adequate photosynthesis conditions (Abowei and Ezekiel, 2013), we primarily investigated the effluent transport in the upper ocean, albeit its substantial 3D behavior crucial to its accumulation in the seaweed farm (Section 3.4). Fig. 3 shows the time-averaged non-dimensional tracer (effluent) concentration c (color) and the seawater density (contours) at the surface from September 21st to October 31st, 2015. The top panel corresponds to Case 1 (the baseline case with $Q_p = 1.8 \times 10^5\,\mathrm{m^3\,d^{-1}}$), while the other two panels represent the deviations for Case 2 (reduced $Q_p = 1.5 \times 10^5\,\mathrm{m^3\,d^{-1}}$, middle) and Case 3 (increased density, bottom), where the deviations are defined as (Case 2 − Case 1) and (Case 3 − Case 1), respectively. Consistent with the residual current field (Fig. 2a), for the baseline case shown in Fig. 3a, the mean effluent concentration c is mostly distributed in the alongshore direction near the TSTP with a pronounced westward bias and suppressed cross-shore

transport. Similar to the c distribution, slight decreases in the surface density occur because of the fresh effluent discharge from the diversion outfall. Another density decrease is observed in the northeastern area of the seaweed farm, and is attributed to both the fresh effluent and to remote influences from major river mouths located in the inner Osaka Bay ~30 km east of the study area (see also Uchiyama et al., 2018a).

The effluent concentration and density surface deviations observed for Case 2 are generally consistent although with opposite signs (Fig. 3b). The surface density ρ slightly increases around the TSTP due to the reduced fresh effluent, while c is diminished. Noticeable modifications in ρ and c are observed only within ~2 km from shore, whereas they extend to the western area of the seaweed farm. Density deviations could dynamically alter the local flow field due to buoyancy effects that may further affect the tracer transport, in addition to the reduced tracer flux at the outfall. In Section 4, the tracer budget analysis to quantify the effects of the reduced tracer flux F_p at the outfall on the seaweed farm is presented. By contrast, the adjusted effluent density with the unchanged total tracer flux (Case 3) does not result in obvious changes in ρ and c, particularly at the seaweed farm, except for the source area (Fig. 3c). We expected for Case 3 that the suppressed surface c from the density change could cause a decrease in the near-surface c transport to the farm, whereas this may not be the case in the present situation where the outfall is located in a very shallow area at 7 m deep. Section 4 also quantifies the effects of the adjusted density changes in the effluent accumulation in the farm.

3.3. Effluent flux budget analysis

A quantitative effluent tracer budget analysis is carried out to evaluate the direct impacts of the TSTP on the seaweed farm for the three cases. Considering a vertical section surrounding the farm with an arbitrary cross-sectional area of A_c, the instantaneous tracer flux F crossing the section is calculated with

$$F(\tau) = \int_{A_c} c u_n dA_c \tag{5}$$

where u_n is the velocity perpendicular to the cross-section, and τ is time. Because c is a non-dimensional concentration, F has the unit of $m^3\,s^{-1}$. Then, we integrate F over a given time period to evaluate the cumulative tracer flux Q (m^3) for the duration from $\tau = 0$ to t as follows:

$$Q(t) = \int_0^t F(\tau) d\tau \tag{6}$$

where the incoming cumulative tracer fluxes into the farm are defined as positive at each of the four sections surrounding the farm as represented by blue lines in Fig. 1c. Hence, the sum of Q at the four vertical cross-sections identifies the net tracer (effluent) flux Q_{farm} accumulated in the seaweed farm, i.e., $Q_{farm} = Q_w + Q_n + Q_e + Q_s$, where Q_w, Q_n, Q_e, and Q_s are the cumulative fluxes $Q(t)$ through the western, northern, eastern, and southern sections, respectively. To distinguish Q_{farm} for the three cases, we denote the net flux as Q_1, Q_2, and Q_3 for Q_{farm} for Cases 1, 2, and 3.

Fig. 4a shows the net cumulative tracer temporal variability in the seaweed farm for the three cases. As time progressed from the initial state with no effluent, the released effluent from the TSTP gradually accumulates in the farm, with apparent tidal and subtidal variabilities in all three cases. Q_1 and Q_3 have similar fluctuations, although Q_2 deviates from the others later in the experiments. The result is consistent with the time-averaged surface tracer concentrations shown in Fig. 3, whereas c is significantly reduced in Case 2. Nevertheless, the increased effluent density in Case 3 does not appreciably influence the effluent accumulation in the farm. Fig. 4b shows the Q_{farm} differences of Cases 2 and 3 from Q_1, in which we denote $\Delta Q_{21} = Q_2 - Q_1$ and $\Delta Q_{31} = Q_3 - Q_1$. The differences clearly indicate that the net tracer accumulation is significantly diminished in Case 2 ($\Delta Q_{21} < 0$), while the reduction in Case 3 is subtle ($\Delta Q_{31} \sim 0$). The results are quantitatively summarized in Table 3 for three selected durations from Sept. 21 and their time averages over the experimental period. The averaged net cumulative tracers are determined to be $2.01 \times 10^4\,m^3$, $1.50 \times 10^4\,m^3$, and $1.98 \times 10^4\,m^3$ for Cases 1–3, respectively. The density change in Case 3 is again confirmed to scarcely alter the effluent accumulation. However, the released flux reduction of 16.7% ($1.8 \times 10^5\,m^3d^{-1} \rightarrow 1.5 \times 10^5\,m^3d^{-1}$) at the diversion outfall in Case 2 results in a 25.4% reduction ($2.01 \times 10^4\,m^3 \rightarrow 1.50 \times 10^4\,m^3$) in the effluent accumulation in the farm relative to Case 1. These results firmly indicate that the complicated currents and associated dispersal near the TSTP have nonlinear influences on total tracers released at the outfall. As shown in Fig. 4a, the Q_{farm} (Q_1, Q_2, and Q_3) variability is dominated by low-frequency subtidal fluctuations that yield Q_{farm} peaks on October 3, 17, and 21, thus occurs at a period of ~14 days. This periodic behavior indicates that intrusion of the sewage effluent into the seaweed farm occurs mainly at a spring–neap tidal cycle. Consistent with the mean accumulations, Table 3 shows that the Q_{farm} peaks for these three days are $1.84 \times 10^4\,m^3$, $3.67 \times 10^4\,m^3$, and $5.49 \times 10^4\,m^3$ for Case 1, $1.60 \times 10^4\,m^3$, $2.78 \times 10^4\,m^3$, and $4.15 \times 10^4\,m^3$ for Case 2, and $1.85 \times 10^4\,m^3$, $3.66 \times 10^4\,m^3$, and $5.22 \times 10^4\,m^3$ for Case 3. In summary, the decreased source flux in Case 2 is more efficient than expected for reducing the effluent in the farm, whereas the density changes in Case 3 are not very efficient in the present configuration.

Table 3
Cumulative non-dimensional tracer fluxes in the seaweed farm, Q_{farm} (m^3).

	Up to Oct. 3rd	Up to Oct. 17th	Up to Oct. 31th	Average
Q_1	1.84×10^4	3.67×10^4	5.49×10^4	2.01×10^4
Q_2	1.60×10^4	2.78×10^4	4.15×10^4	1.50×10^4
Q_3	1.85×10^4	3.66×10^4	5.22×10^4	1.98×10^4
ΔQ_{21}	-0.24×10^4	-0.89×10^4	-1.34×10^4	-0.51×10^4
ΔQ_{31}	0.1×10^4	-0.01×10^4	-0.27×10^4	-0.03×10^4

Note: $\Delta Q_{21} = Q_2 - Q_1$, $\Delta Q_{31} = Q_3 - Q_1$.

3.4. Effects of the mean and transient flow components on the tracer fluxes

The counterclockwise residual Tarumi Recirculation formed off the TSTP (Fig. 2a) is anticipated to contribute to a 25.4% reduction in the effluent accumulation in the farm due to the 16.7% decrease in the input flux. However, as long as the residual current field is not altered by the reduced fresh effluent flux from the outfall, the nonlinear

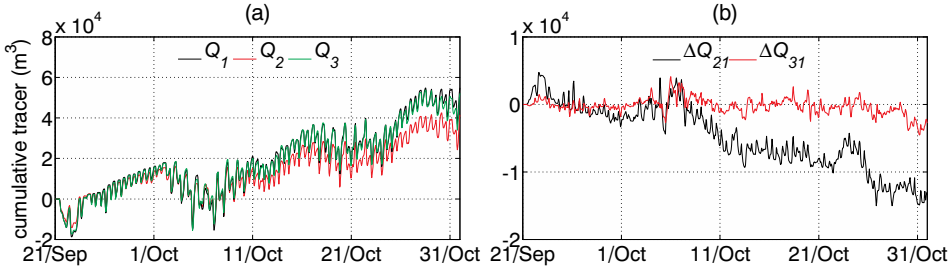

Fig. 4. (a) Time series of the temporally cumulative net tracer fluxes stored in the seaweed farm area, Q_{farm} (m^3). The black, red and green curves show Q_1, Q_2 and Q_3 for Cases 1, 2, and 3, respectively. Note that Q_1 nearly coincides with Q_3. (b) The temporal changes in the Q_{farm} (m^3) differences for each case. The black curve ΔQ_{21} is for Case 2 − Case 1, while the red curve ΔQ_{31} is for Case 3 − Case 1. (For interpretation of the references to color in this figure legend, the reader is referred to the web version of this article.)

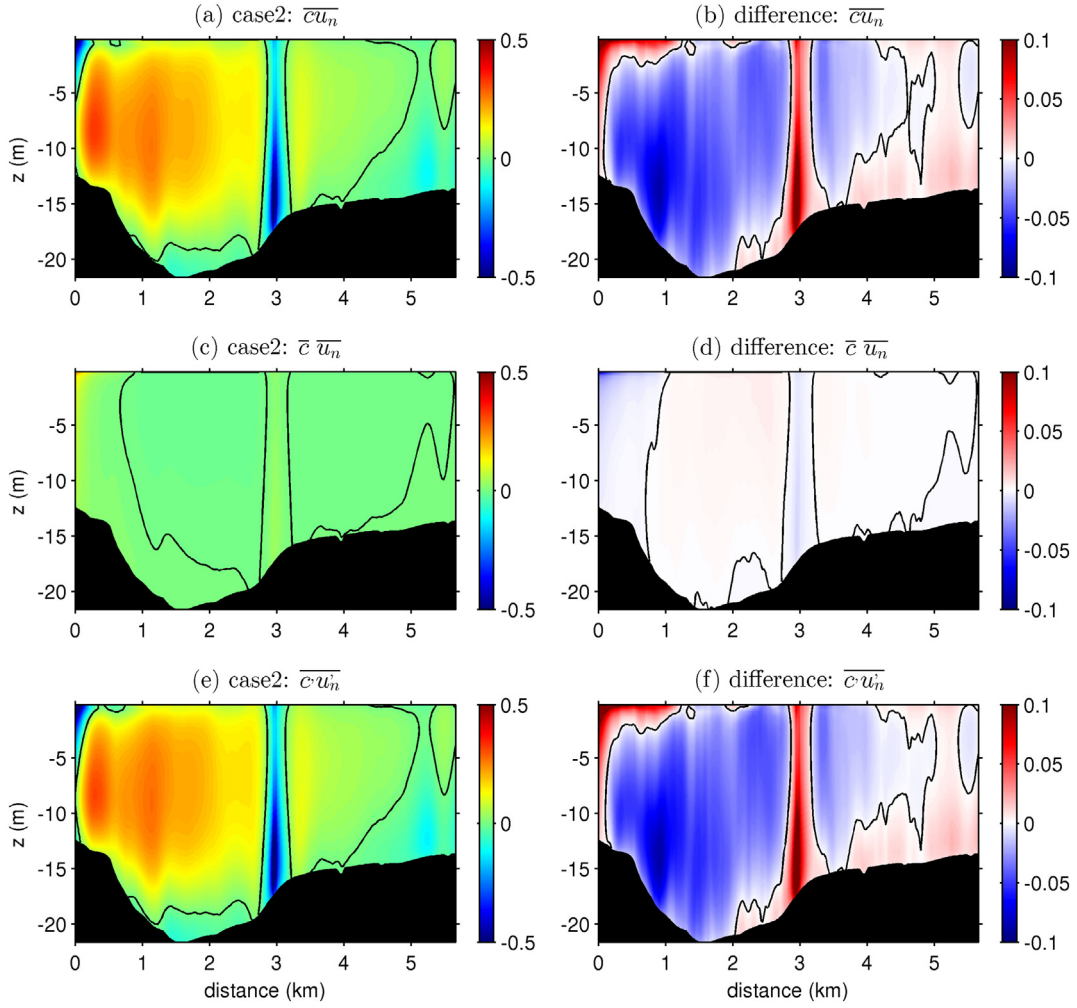

Fig. 5. Cross-sectional distributions of (a) the time-averaged flux $\overline{cu_n}$ ($m^3\,h^{-1}$), (c) the mean linear component $\overline{c}\ \overline{u_n}$ ($m^3\,h^{-1}$), and (e) the transient flow component $\overline{c'u_n'}$ ($m^3\,h^{-1}$) at the northern boundary of the seaweed farm for Case 2, (b), (d) and (f) show the difference of $\overline{cu_n}$ $\overline{c}\ \overline{u_n}$ and $\overline{c'u_n'}$ between Case 2 and Case 1 (Case 2 − Case 1). The black contours denote 0.

influence observed in Case 2 may rarely occur. To examine the possible mechanism behind the nonlinearity, we introduce a Reynolds decomposition to the prognostic variables for the mean and transient components, in which $c = \overline{c} + c'$ and $u_n = \overline{u_n} + u_n'$. Therefore, the time-averaged tracer flux $\overline{cu_n}$ is decomposed as

$$\overline{cu_n} = \overline{c}\ \overline{u_n} + \overline{c'}\ \overline{u_n} + \overline{c}\overline{u_n'} + \overline{c'u_n'} = \overline{c}\ \overline{u_n} + \overline{c'u_n'} \quad (7)$$

where the overbar denotes an ensemble (time) averaging operator, and the prime represents the transient component that is the deviation from the ensemble mean and explains fluctuations associated mostly with eddies and tides. The first term $\overline{c}\ \overline{u_n}$ on the right hand side represents the linear interaction of the mean tracer concentration $\overline{c}$ and residual currents $\overline{u_n}$, whereas the second term $\overline{c'u_n'}$ denotes the tracer flux associated with the nonlinear interaction of the transient currents u_n' with the instantaneous tracer concentration c'. Note that the high-frequency turbulent components are included in the transient component, although they are subtle as compared to tidal and subtidal eddy components (Uchiyama et al., 2018a).

Fig. 5 illustrates the cross-sectional distributions of the time-averaged flux $\overline{cu_n}$ ($m^3\,h^{-1}$, top panels), the mean linear component $\overline{c}\ \overline{u_n}$ (middle panels), and the nonlinear transient component $\overline{c'u_n'}$ (bottom panels) along the northern boundary of the seaweed farm from September 21st to October 31st, 2015. For Case 2 (left column) and the deviations from those for Case 1 (Case 2 − Case 1, right column). As u_n is the velocity component normal to the northern section, Fig. 5 principally depicts the cross-shore tracer transport, where the positive flux denotes the incoming flux into the farm. The total flux $\overline{cu_n}$ is generally positive, indicating an overall southward intrusion of the TSTP-derived effluent into the farm. In particular, this occurs in the western area ~3 km from the northwestern corner of the farm (Fig. 5a, warm color), even though the westward residual current is formed as a part of the counter-clockwise circulation in this location (Fig. 2a). An observable opposing outgoing flux occurs locally around the middle part of the northern section (cold color) that is most likely caused by the influences from the fishing pier (Fig. 2b). The reduced source tracer flux in Case 2 successfully causes an overall reduction in the incoming flux $\overline{cu_n}$ (Fig. 5b). The decomposed flux components (Fig. 5c, e) and their differences from those in Case 1 (Fig. 5d, f) demonstrate the striking predominance of the transient component $\overline{c'u_n'}$ over the mean component $\overline{c}\ \overline{u_n}$. The mean component is slightly negative because of the outgoing northward residual currents formed along the northern section (e.g., Fig. 2b). Nevertheless, the nonlinear transient flux plays a dominant role in the overall incoming flux and its reduction associated with the decreased source flux in Case 2 (Fig. 5e, f). The superiority of the transient component over the mean component is also observed in the southern cross-section of the farm, albeit with an outflux dominance in that location (not shown). It should be noted that Uchiyama et al. (2018a) showed that a net effluent accumulation occurs in the alongshore direction with persistent incoming effluent fluxes both along the western and eastern sections, while a net reduction occurs in the cross-

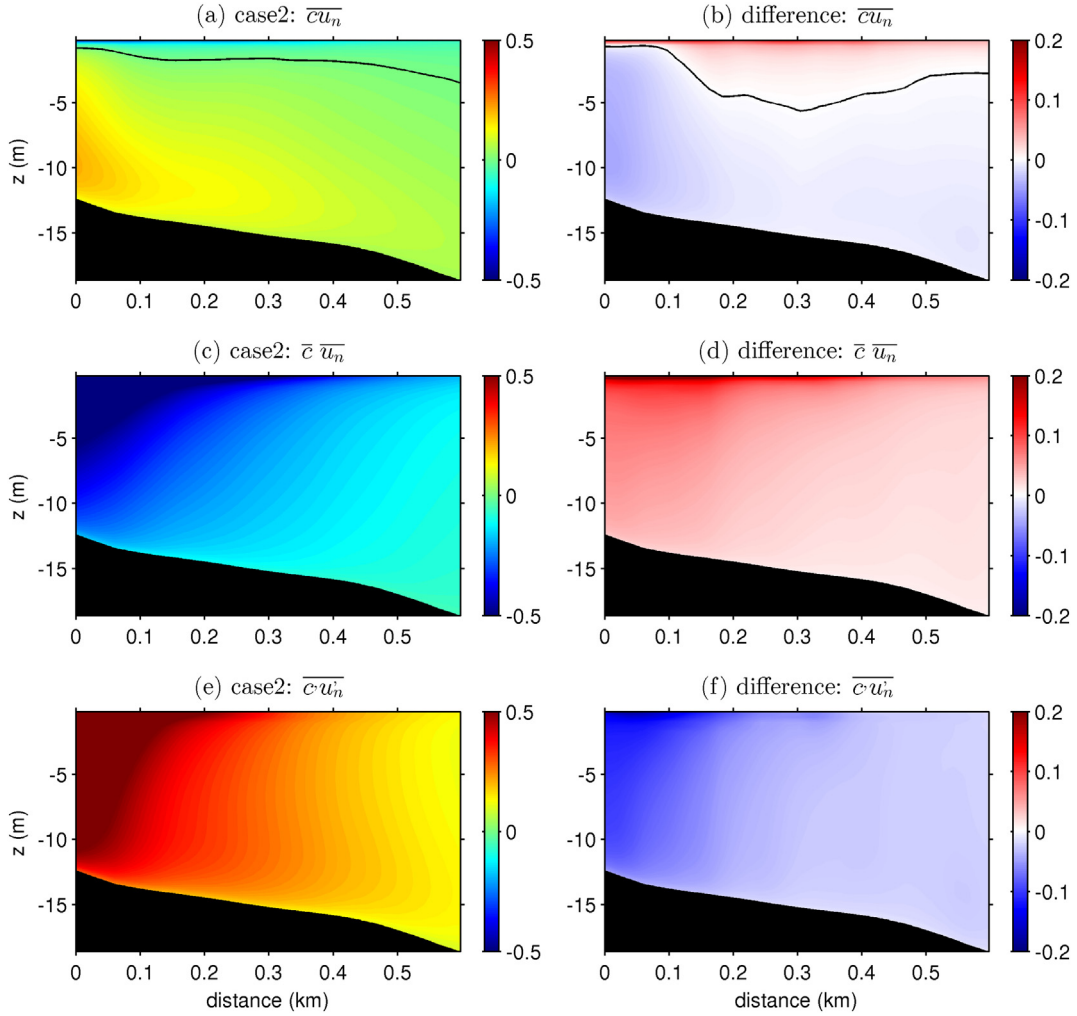

Fig. 6. Same as Fig. 5, but for the western cross-section of the seaweed farm.

shore direction due to the prevailing outgoing effluent fluxes from the southern section.

Fig. 6 is the same as Fig. 5, except that it shows the western cross-section of the seaweed farm. Note that the depicted fluxes are mainly the alongshore tracer transport as u_n becomes the normal component in the western section. The Case 2 time-averaged tracer flux $\overline{cu_n}$ (Fig. 6a) shows that the flux of the discharged effluent is largely positive (flowing into the farm represented by warm colors) and occurs more intensively in the lower layer peaking at around $z = -10$ m in the northern part of the cross-section closer to the TSTP, while it is rather outgoing near the surface (cold colors). As compared to the baseline case, Case 2 results in an increased tracer influx near the surface and a reduction in the deep layer (Fig. 6b). The contributions from the mean linear components $\bar{c}\ \overline{u_n}$ and the transient nonlinear components $\overline{c'u_n'}$ (Fig. 6c, e) are completely different from those along the northern section shown in Fig. 5c, e. Both components are similar in magnitude, but with opposite signs. Although $\overline{c'u_n'}$ is generally positive for inducing overall incoming tracer fluxes into the farm, $\bar{c}\ \overline{u_n}$ counteracts to extract the effluent from the farm. The negative $\bar{c}\ \overline{u_n}$ is apparently attributed to the westward residual current in front of the TSTP (Fig. 2a). However, as compared to Case 1, $\bar{c}\ \overline{u_n}$ enhances the effluent accumulation in the farm (Fig. 6d), while $\overline{c'u_n'}$ depresses effluent intrusion into the farm (Fig. 6f). The resultant net effects of the reduced source flux at the outfall (Case 2) are to overall reduce effluent accumulation in the farm (Fig. 6b). By contrast, at the eastern transect, the mean $\bar{c}\ \overline{u_n}$ leads to an increased influx, while the transient $\overline{c'u_n'}$ reduces the accumulation in Case 2 relative to Case 1 (not shown). Nevertheless, the eastern section is located farthest from the outfall and thus the effluent influx along this section on the net tracer budget was subtle.

The present tracer budget analysis provides important insights into the assessment of this type of treatment plant operations. Synchronous observation of the transient currents and effluent concentrations is crucial for proper flux estimations, yet such observations are laborious. A simple multiplication of the residual currents and mean concentrations could yield an incorrect effluent flux, where nonlinear interactions between the transient currents and concentrations generate predominant mean fluxes through their interactions. Moreover, the significance of $\overline{c'u_n'}$ arises differently in the alongshore and cross-shore effluent transports. The residual counterclockwise circulation that transports the effluent away from the farm largely affects the seaweed farm near the TSTP, although the nonlinear transient flux brings more complexity to the mechanism.

4. Conclusions

A well-validated, multi-nested, high-resolution, synoptic ocean circulation model coupled with a 3D Eulerian passive tracer model (Uchiyama et al., 2014, 2018a) was utilized to assess the impacts of wastewater effluents in the standard diversion and two alternative scenarios at the TSTP on an adjacent seaweed farm located near the narrow Akashi Strait. We discovered that in the reduced flux case (Case 2), 16.7% of the wastewater discharge rate decreased from the standard diversion operation ($1.8 \times 10^5\ m^3\ d^{-1} \rightarrow 1.5 \times 10^5\ m^3\ d^{-1}$) resulted in an overall 25.4% reduction in the sewage effluent accumulating on

average in the seaweed farm ($2.01 \times 10^4\ m^3 \rightarrow 1.50 \times 10^4\ m^3$). The effluent reduction at the farm was more than expected and was not linearly proportional to the reduced source flux with this particular configuration (Case 2). We need to conduct more model cases to ensure it in future. In turn, the addition of ambient seawater to the freshwater effluent to adjust the source density (Case 3) did not substantially alter the effluent accumulation and associated hydrodynamics at the farm because of the shallow bottom-mounted outfall (~7 m depth). A Reynolds decomposition demonstrated that the transient flux played a dominant role over the mean component in the effluent accumulation in the farm, more evidently in the cross-shore transport than the alongshore transport. When the source effluent flux was reduced, the transient component remarkably depressed the southward influx at the northern boundary of the seaweed farm. In contrast, in the along-shore direction, the mean and transient components competed with each other, leading to comparable effluent outfluxes and influxes, respectively. As a result, the net influx emerged along the western boundary of the farm, that was also decreased by the reduced source effluent flux. Evidently, a key influencer on the effluent budget was the mean westward residual current developed off the TSTP as a part of the counterclockwise Tarumi Recirculation. In turn, the transient flux counteracts the mean component to promote the incoming effluent flux and thus the accumulation in the farm. Nevertheless, its contribution becomes more prominent and acts to significantly reduce the influx when the source effluent flux was reduced.

Acknowledgements

This study was financially supported by the City of Kobe and the Japan Society for the Promotion of Science (JSPS) Grants-in-Aid for Scientific Research 15KK0207 and 18H03798 at Kobe University. We also appreciate Yota Suzue (CTI Engineering Co., Ltd.), Taichi Kosako (Port and Airport Research Institute), and Yasumasa Miyazawa (Japan Agency for Marine-Earth Science and Technology) for their help in the development of the quadruple nested ROMS model embedded in the assimilative Japan Coastal Ocean Predictability Experiments (JCOPE2) oceanic reanalysis that was used in the analysis. The effluent data and alternative discharge scenarios for the Tarumi Sewage Treatment Plant were provided by the City of Kobe.

References

Abowei, J.F.N., Ezekiel, E.N., 2013. The potentials and utilization of seaweeds. Sci. Agric. 4 (2), 58–66.

Becker, J.J., Sandwell, D.T., Smith, W.H.F., Braud, J., Binder, B., Depner, J., Fabre, D., Factor, J., Ingalls, S., Kim, S.-H., Ladner, R., Marks, K., Nelson, S., Pharaoh, A., Trimmer, R., Von Rosenberg, J., Wallace, G., Weatherall, P., 2009. Global bathymetry and elevation data at 30 arc seconds resolution: SRTM30_PLUS. Mar. Geod. 32 (4), 355–371. https://doi.org/10.1080/01490410903297766.

Bricker, J.D., Nakayama, A., 2007. Estimation of far-field horizontal and vertical turbulent diffusion coefficients from the concentration field of a wastewater plume near the Akashi Strait. Environ. Fluid Mech. 7, 1–22. https://doi.org/10.1007/s10652-006-9013-4.

Bricker, J.D., Okabe, I., Nakayama, A., 2006. Behavior of a small pulsed river plume in a strong tidal cross-flow in the Akashi Strait. Environ. Fluid Mech. 6, 203–225. https://doi.org/10.1007/s10652-005-3480-x.

Buijsman, M., Uchiyama, Y., McWilliams, J.C., Hill-Lindsay, C.R., 2012. Modeling semidiurnal internal tides in the Sourthern California bight. J. Phys. Oceanogr. 42, 62–77. https://doi.org/10.1175/2011JPO4597.1.

Chang, P.H., Guo, X., Takeoka, H., 2009. A numerical study of the seasonal circulation in the Seto Inland Sea, Japan. J. Oceanogr. 65, 721–736. https://doi.org/10.1007/s10872-009-0062-4.

Egbert, G.D., Erofeeva, S.Y., 2002. Efficient inverse modeling of barotropic ocean tides. J. Atomspher. Ocean. Technol. 19, 183–204. https://doi.org/10.1175/1520-0426(2002)019<0183:EIMOBO>2.0.CO;2.

Egbert, G.D., Bennett, A.F., Foreman, M.G.G., 1994. TOPEX/POSEIDON tides estimated using a global inverse model. J. Geophys. Res. 99, 24821–24852. https://doi.org/10.1029/94JC01894.

Fujiwara, T., Nakata, H., Nakatsuji, K., 1994. Tidal-jet and votex-pair driving of the residual circulation in a tidal estuary. Cont. Shelf Res. 14, 1025–1038. https://doi.org/10.1016/0278-4343(94)90062-0.

Guo, X., Futamura, A., Takeoka, H., 2004. Residual currents in semi-enclosed bay of the Seto Inland Sea. Japan. J. Geophys. Res. 109, C12008. https://doi.org/10.1029/2003JC002203.

Hodur, R.M., 1997. The naval research laboratory's coupled ocean/atmosphere mesoscale prediction system (COAMPS). Monthly Weath. Rev. 125, 1414–1430. https://doi.org/10.1175/1520-0493(1997)125<1414:TNRLSC>2.0.CO;2.

Imai, I., Yamaguchi, M., Hori, Y., 2006. Eutrophication and occurrences of harmful algal blooms in the Seto Inland Sea, Japan. Plankt. Benth. Res. 1 (2), 71–84. https://doi.org/10.3800/pbr.1.71.

Imasato, N., 1983. A numerical experiment on water and salt exchange through the Akashi and Naruto Straits. J. Phys. Oceanogr. 13, 1526–1533. https://doi.org/10.1175/1520-0485(1983)013<1526:ANEOWA>2.0.CO;2.

Imasato, N., Fujo, S., Zhang, Q., Awaji, T., Akitomo, K., 1994. Three-dimensional numerical experiments on tidal exchange through a narrow strait in a homogeneous and a stratified sea. J. Oceanogr. 50, 119–139. https://doi.org/10.1007/BF02253474.

Irizuki, T., Hirose, K., Ueda, Y., Fujihara, Y., Ishiga, H., Seto, K., 2018. Ecological shifts due to anthropogenic activities in the coastal seas of the Seto Inland Sea, Japan, since the 20th century. Mar. Pollut. Bull. 127, 637–653. https://doi.org/10.1016/j.marpolbul.2017.12.050.

Isoguchi, O., Shimada, M., Kawamura, H., 2010. Characteristics of ocean surface winds in the lee of an isolated island observed by synthetic aperture radar. Monthly Weath. Rev. 139, 1744–1761. https://doi.org/10.1175/2010MWR3564.1.

Kamidaira, Y., Uchiyama, Y., Mitarai, S., 2017. Eddy-induced transport of the Kuroshio warm water around the Ryukyu Islands in the East China Sea. Cont. Shelf Res. 143, 206–218. https://doi.org/10.1016/j.csr.2016.07.004.

Kamidaira, Y., Uchiyama, Y., Kawamura, H., Kobayashi, T., Furuno, A., 2018. Submesoscale mixing on initial dilution of radionuclides released from the Fukushima Daiichi Nuclear Power Plant. J. Geophys. Res. Oceans. 123, 2808–2828. https://doi.org/10.1002/2017JC013359.

Kawabe, M., 1987. Spectral properties of sea level and time scale of Kuroshio path variations. J. Oceanogr. Society Japan 43, 111–123. https://doi.org/10.1007/BF02111887.

Kawabe, M., 1995. Variations of current path, velocity, and volume transport of the Kuroshio in relation with the large meander. J. Phys. Oceanogr. 25, 3103–3117. https://doi.org/10.1175/1520-0485(1995)025<3103:VOCPVA>2.0.CO;2.

Li, Y., Wolanski, E., Zhang, H., 2015. What processes control the net currents through shallow straits? A review with application to the Bohai Strait, China. Estuar. Coast. Shelf Sci. 158, 1–11. https://doi.org/10.1016/j.ecss.2015.03.013.

Mason, E., Molemake, J., Shchepetkin, A.F., Colas, F., McWilliams, J.C., Sangrà, P., 2010. Procedures for offline grid nesting in regional ocean models. Ocean Modell 35, 1–15. https://doi.org/10.1016/j.ocemod.2010.05.007.

Mishima, Y., Hoshika, A., Tanimoto, T., 1999. Deposition rates of terrestrial and marine organic carbon in the Osaka Bay, Seto Inland Sea, Japan, determined using carbon and nitrogen stable isotope rations in the sediment. J. Oceanogr. 55, 1–11. https://doi.org/10.1023/A:1007850003262.

Miyazawa, Y., Zhang, R., Guo, X., Tamura, H., Ambe, D., Lee, J., Okuno, A., Yoshinari, H., Setou, T., Komatsu, K., 2009. Water mass variability in the Western North Pacific detected in 15-year Eddy Resolving Ocean reanalysis. J. Oceanogr. 65, 737–756. https://doi.org/10.1007/s10872-009-0063-3.

Nakatsuji, K., Fujiwara, T., Kurita, H., 1994. An estuarine system in semi-enclosed Osaka Bay in Japan. In: Dyer, K.R., Orth, R.J. (Eds.), Changes in Fluxes in Estuaries: Implications from Science to Management, ECSA22/EFR Symposium. Olsen & Olsen, Fredensborg, Denmark, pp. 79–84.

Rodriguez, E., Morris, J.E., Belz, J.E., Chapin, E.C., Martin, J.M., Daffer, W., Hensley, S., 2005. An Assessment of the SRTM Topographic Products. Technical Report. Jet Propulsion Laboratory, Pasadena, CA.

Rodriguez, E., Morris, C.S., Belz, J.E., 2006. A global assessment of the SRTM performance. Photogramm. Eng. Rem. Sens. 72 (3), 249–260. https://doi.org/10.14358/PERS.72.3.249.

Romero, L., Uchiyama, Y., Ohlmann, C., McWilliams, J.C., Siegel, D.A., 2013. Simulations of nearshore particle-pair dispersion in Southern California. J. Phys. Oceanogr. 43, 1862–1879. https://doi.org/10.1175/JPO-D-13-011.1.

Shchepetkin, A.F., McWilliams, J.C., 2005. The regional ocean modeling system (ROMS): a split-explicit, free-surface, topography-following-coordinate oceanic model. Ocean Modell 9, 347–404. https://doi.org/10.1016/j.ocemod.2004.08.002.

Shchepetkin, A.F., McWilliams, J.C., 2008. Computational kernel algorithms for fine-scale, multiprocess, longtime oceanic simulations. In: Temam, R., Tribbia, J. (Eds.), Handbook of Numerical Analysis: Computational Methods for the Ocean and the Atmosphere. Elsevier, Amsterdam, pp. 119–181. https://doi.org/10.1016/S1570-8659(08)01202-0.

Tada, H., Uchiyama, Y., Masunaga, E., 2018. Impacts of two super typhoons on the Kuroshio and marginal seas off the Pacific coast of Japan. Deep-Sea Res. Part I. 132, 80–93. https://doi.org/10.1016/j.dsr.2017.12.007.

Takeoka, H., Akiyama, H., Kikuchi, T., 1993. The Kyucho in the Bungo Channel, Japan-periodic intrusion of oceanic warm water. J. Oceanogr. 49, 369–382. https://doi.org/10.1007/BF02234954.

Terawaki, T., Yoshikawa, K., Yoshida, G., Uchimura, M., Iseki, K., 2003. Ecology and restoration techniques for Sargassum beds in the Seto Inland Sea, Japan. Mar. Pollut. Bull. 47, 198–201. https://doi.org/10.1016/S0025-326X(03)00054-7.

Tomita, A., Nakura, Y., Ishikawa, T., 2016. New direction for environmental water management. Mar. Pollut. Bull. 102, 323–328. https://doi.org/10.1016/j.marpolbul.2015.07.068.

Uchiyama, Y., McWilliams, J.C., Shchepetkin, A.F., 2010. Wave-current interaction in an oceanic circulation model with a vortex force formalism: application to the surf zone. Ocean Model 34 (1–2), 16–35. https://doi.org/10.1016/j.ocemod.2010.04.002.

Uchiyama, Y., Idica, E.Y., McWilliams, J.C., Stolzenbach, K.D., 2014. Wastewater effluent dispersal in Southern California bays. Cont. Shelf Res. 76, 36–52. https://doi.org/10.1016/j.csr.2014.01.002.

Uchiyama, Y., Suzue, Y., Yamazaki, H., 2017a. Eddy-driven nutrient transport and associated upper-ocean primary production along the Kuroshio. J. Geophys. Res. Oceans 122, 5046–5062. https://doi.org/10.1002/2017JC012847.

Uchiyama, Y., Kanki, R., Takano, A., Yamazaki, H., Miyazawa, Y., 2017b. Mesoscale reproducibility in regional ocean modelling with a three-dimensional stratification estimate based on Aviso-Argo data. Atmosphere-Ocean 55, 1–18. https://doi.org/10.1080/07055900.2017.1399858.

Uchiyama, Y., McWilliams, J.C., Akan, C., 2017c. Three-dimensional transient rip currents: bathymetric excitation of low-frequency intrinsic variability. J. Geophys. Res. Oceans 122, 5826–5849. https://doi.org/10.1002/2017JC013005.

Uchiyama, Y., Zhang, X., Suzue, Y., Kosako, T., Miyazawa, Y., Nakayama, A., 2018a. Residual effects of treated effluent diversion on a seaweed farm in a tidal strait using a multi-nested high-resolution 3-D circulation-dispersal model. Mar. Pollut. Bull. 130, 40–54. https://doi.org/10.1016/j.marpolbul.2018.03.007.

Uchiyama, Y., Odani, S., Kashima, M., Kamidaira, Y., Mitarai, S., 2018b. Influences of the Kuroshio on interisland remote connectivity of corals across the Nansei Archipelago in the East China Sea. J. Geophys. Res. Oceans. 123, 9245–9265. https://doi.org/10.1029/2018JC014017.

Woodruff, S.D., Slutz, R.J., Jenne, R.L., Steurer, P.M., 1987. A comprehensive ocean-atmosphere data set. Bull. American Meteorolog. Soc. 68, 1239–1250. https://doi.org/10.1175/1520-0477(1987)068<1239:ACOADS>2.0.CO;2.